EUROfusion

WPMST1-PR(18) 20032

S Ratynskaia et al.

Interaction of metal dust adhered on castellated substrates with the ELMy H-mode plasmas of ASDEX-Upgrade

Preprint of Paper to be submitted for publication in Nuclear Fusion

This work has been carried out within the framework of the EUROfusion Consortium and has received funding from the Euratom research and training programme 2014-2018 under grant agreement No 633053. The views and opinions expressed herein do not necessarily reflect those of the European Commission.

Interaction of metal dust adhered on castellated substrates with the ELMy H-mode plasmas of ASDEX-Upgrade

S. Ratynskaia,[1] P. Tolias,[1] M. De Angeli,[2] V. Rohde,[3] A. Herrmann,[3] D. Ripamonti,[4] G. Riva,[4] E. Thorén,[1] L. Vignitchouk,[1] B. Sieglin,[3] K. Krieger,[3] R. Neu,[3] the ASDEX-Upgrade Team[3] and the EUROfusion MST1 Team[5*]

[1] *Space and Plasma Physics - KTH Royal Institute of Technology, SE-10044, Stockholm, Sweden*

[2] *Istituto di Fisica del Plasma - Consiglio Nazionale delle Ricerche, 20125, Milan, Italy*

[3] *Max-Planck-Institut für Plasmaphysik, 85748, Garching b. München, Germany*

[4] *Institute of Condensed Matter Chemistry and Energy Technologies - Consiglio Nazionale delle Ricerche, 20125, Milan, Italy*

[5] *EUROfusion Programme Management Unit, 85748, Garching b. München, Germany*

Castellated substrates with adhered micron dust have been exposed in the outer ASDEX-Upgrade divertor to ELMy H-mode discharges. Beryllium proxy (chromium, copper) and refractory metal (tungsten, molybdenum) dust has been deposited on the plasma-facing and plasma-shadowed sides of the monoblocks as well as the bottom of the gaps. Interaction with time-averaged transient heat loads up to $5\,\mathrm{MW/m^2}$ led to dust remobilization, clustering, melting and wetting-induced coagulation. The amount of dust released in the vessel has been quantified and remobilized dust trajectories inferred. Gaps can efficiently trap locally adhered dust, but dust detaching from adjacent monoblocks does not preferentially move inside the gaps implying that they do not constitute a dust accumulation site. Heat transfer simulations of melting events are also reported taking into account heat constriction due to the finite contact area and the presence of surface roughness.

I. INTRODUCTION

ITER nuclear licensing imposes an upper limit on the quantity of dust permissible in the vacuum vessel [1–3], which is more stringent for dust residing on hot surfaces due to the explosion hazard in case of loss-of-coolant accidents [4]. Dust accumulation on the plasma-facing components (PFCs) of fusion devices depends on the global balance between generation and destruction as well as the local balance between sticking and remobilization. Experimental and computational works have focused on droplet formation and subsequent release [5–10], whereas dust transport and vaporization have been investigated with numerical codes modelling the exchange of charge, mass, momentum and energy of single particulates with the surrounding plasma [11, 12]. Dust sticking and mechanical impacts with PFCs have also been incorporated in dust dynamics codes [12, 13], whereas the process of remobilization has only recently received attention, mainly in the form of experiments with tungsten dust [14–19].

Steady state remobilization experiments revealed the higher remobilization tendency of larger dust and clusters but also the statistical nature of the process owing to surface roughness [14, 16, 17]. Transient plasma remobilization experiments revealed the generation of larger dust through wetting-induced coagulation, the enhanced survivability of dust on hot surfaces (albeit with macromorphological changes) and the inhibition of remobilization at elevated temperatures due to contact strengthening [15, 16, 18]. The aforementioned experiments mainly involved W dust adhered to planar W substrates in a controlled manner, these samples were exposed to the boundary plasmas of the TEXTOR, DIII-D and COMPASS tokamaks as well as the linear plasmas of the Pilot-PSI device. Despite the progress, several aspects remain to be addressed that are specific to the ITER-wall geometry and composition. These mainly concern: (i) the interaction of adhered beryllium dust with edge-localized modes (ELMs) and its remobilization tendency, since Be is expected to be the main dust constituent in ITER, (ii) the effect of the castellated PFC geometry on the trajectories of remobilized dust and the efficiency of gaps in the trapping of locally amassed dust, *i.e.* the evaluation of whether gaps constitute a dust accumulation site.

Aiming to investigate these issues, refractory metal dust (W, Mo) and Be proxy dust (Cu, Cr) has been adhered to castellated W substrates and exposed to ELMy H-mode ASDEX-Upgrade (AUG) discharges taking advantage of the divertor manipulator system DIM-II [20]. After the AUG transition to a full-metal first wall, there have been numerous dust investigations comprising of the post-mortem analysis of the size, morphology and composition of collected dust [21–23] as well as the fast camera analysis of the trajectories of intrinsic dust [24, 25]. In spite of the systematic dust activities, this is the first time that calibrated extrinsic dust has been intentionally introduced in AUG.

Dust was adhered to the castellated W substrates at multiple predetermined deposition spots located on the top (plasma-facing) monoblock surface, side monoblock surface and bottom gap surface. Overall, five castellated samples each containing twelve dust spots were exposed under different plasma conditions (incident heat flux, exposure time, number of discharges). The strong statistics allowed for the quantification of the remobilization activity and the melting occurrence. Heat transfer simulations of adhered dust melting events are also reported taking into account heat constriction due to the finite contact area and the presence of surface roughness.

---

*See author list of Ref.[62].

II. EXPERIMENTAL REALIZATION

A. Castellated samples

The design characteristics of the DIM-II introduction system imposed some restrictions on the dimensions of the castellated samples which did not exactly match the ITER specifications. The castellated structures consisted of two identical unshaped (non-chamfered) W monoblocks of 33.5 mm poloidal length, 5.75 mm toroidal width and 2.0 mm radial height. The two W monoblocks were joined to a common W baseplate via a shallow tail lock. The toroidal gap was 0.5 mm wide and only 2.0 mm deep. Geometrical details are depicted in Fig.1, together with the dimensions of the constituents.

In contrast to the W baseplate, the surface roughness characteristics of the manufactured W monoblocks did not comply with the original technical specifications. In the top (plasma wetted) and side (plasma shadowed) surfaces of the monoblocks, the surface texture was rather inhomogeneous featuring numerous large-scale irregularities such as cracks, pits and protrusions. Consequently, for the top and side surfaces, the roughness measures exhibited quite strong variations even within different regions of the same monoblock. Therefore, the measured values quoted below are averages acquired from different regions that should be treated as indicative. For the baseplate, the root-mean-square and arithmetic mean roughness measures were $R_q \simeq 160\,\text{nm}$ and $R_a \simeq 120\,\text{nm}$, respectively. For the top monoblock surface we have the ranges $R_q \simeq 500 - 1200\,\text{nm}$ and $R_a \simeq 300 - 900\,\text{nm}$, whereas for the side monoblock surface we have the ranges $R_q \simeq 1000 - 1400\,\text{nm}$ and $R_a \simeq 600 - 900\,\text{nm}$. Finally, we note that the occurrence of the surface irregularities was much more frequent in the side surfaces, to the degree that it inhibited the image analysis for the smallest dust sizes deposited.

B. Dust deposition

Controlled dust adhesion on the castellated samples was achieved with a pneumatic system, employed in our previous experimental studies of dust remobilization (see Ref.[14] for a detailed description). The system accelerates a plastic sphere of 4 mm diameter up to a measured speed (in the range of $2 - 3\,\text{m/sec}$ for the present experiments) towards the deposition surface. The accelerated carrier is preemptively loaded with the desired dust population. The surface is encased in appropriately masked holders featuring circular holes (0.5 mm diameter, 4 mm spacing) that lead to the deposition patterns of Fig.2b. Dust is released upon the collision of the carrier with the holder and impacts on the deposition surface after passing through the holes. Its impact velocity lies below the sticking threshold resulting in adhesion to the surface.

Two different composition types were considered for the deposited dust; refractory metals (W, Mo) and beryllium proxies (Cu, Cr). The refractory dust populations had the following characteristics: **(i)** perfectly spherical W dust of a nominal size distribution $5 - 25\,\mu\text{m}$ and an average diameter of $\sim 10\,\mu\text{m}$ supplied by TEKNA Advanced Materials Inc, **(ii)** nearly monodisperse spherical W dust with an average diameter of $\sim 14\,\mu\text{m}$ meshed out from the polydisperse batch with the aid of precision sieves and ultrasonic cells, **(iii)** irregular W dust of a nominal size distribution $\lesssim 1\,\mu\text{m}$, but an actual $\lesssim 5\,\mu\text{m}$ distribution with an average diameter of $\sim 2\,\mu\text{m}$, supplied by Tungsteno S.n.c., **(iv)** nearly monodisperse spherical Mo dust with an average diameter of $\sim 14\,\mu\text{m}$ meshed out from a nominal $15-45\,\mu\text{m}$ polydisperse batch supplied by TEKNA Advanced Materials Inc. The beryllium proxy dust populations had the following character-

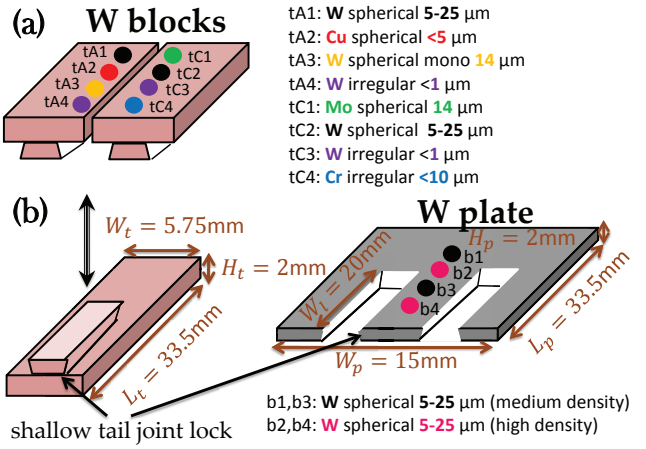

FIG. 1: Sketch of the castellated structures for the case of the top-top deposition (W07-W10). Topology of the dust spots together with the dust composition, shape and nominal size ranges for the (a) top-top surfaces, (b) bottom surface.

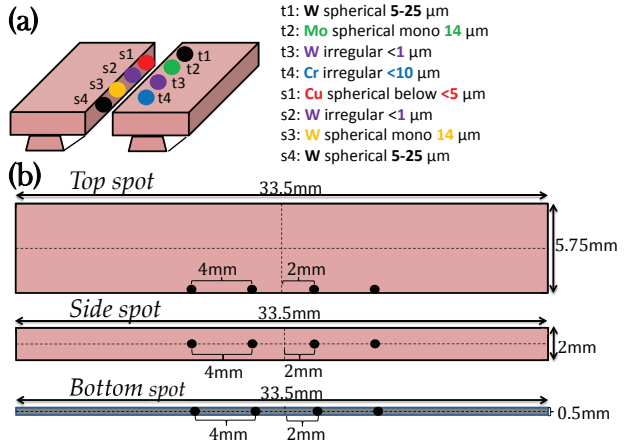

FIG. 2: (a) Sketch of the castellated structures for the case of the top-side deposition (W06). Topology of the dust spots together with the dust composition, shape and nominal size ranges for the top-side surfaces. Dust deposition at the bottom surface is the same as in Fig.1b. (b) Scaled geometry of the top, side and bottom spots.

istics: **(i)** nearly spherical Cu dust of a nominal size distribution $\lesssim 5\,\mu$m and an average diameter of $\sim 3\,\mu$m supplied by Goodfellow Cambridge Ltd, **(ii)** highly irregular (flaky) Cr dust of a nominal size distribution $\lesssim 10\,\mu$m and an average equivalent diameter of $\sim 5\,\mu$m supplied by Goodfellow Cambridge Ltd. We point out that beryllium possesses a rather unique set of thermomechanical properties (thermal conductivity, specific heat capacity, melting point, Young's modulus, yield strength, surface energy). Therefore, it has not been possible to identify a single thermomechanical proxy. Cr was considered to be a suitable tokamak-compatible mechanical proxy and Cu a suitable tokamak-compatible thermal proxy.

These dust populations were deposited on the top monoblock surface, the side monoblock surface and the bottom of the gaps. Sets of four dust spots of well-defined edges were deposited on each surface, to be referred to as top, side and bottom spots, respectively. The topology of the dust spots together with the corresponding dust populations are detailed in Fig.1a,b and Fig.2a. The geometrical characteristics of the dust spots reflect the geometrical characteristics of the masked holders, *i.e.* circular spots of 0.5 mm diameter and 4 mm spacing, see Fig.2b. All the spots were pre-mapped by means of a scanning electron microscope (SEM). Wide optical investigations of the whole castellated samples were also performed in order to verify that prior to exposure dust was confined exclusively within the deposition spots.

Five castellated samples have been exposed to AUG discharges, labelled as W06-W10. All samples featured a set of bottom spots (Fig.1b), samples W07-W10 also featured two sets of top spots (top-top deposition, Fig.1a), sample W06 also featured a set of top spots and a set of side spots (top-side deposition, Fig.2a). Five castellated samples have been prepared for contingency that were not exposed (all with top-top deposition). They served as reference samples, verifying that transportation did not cause any differences in the dust deposition profiles.

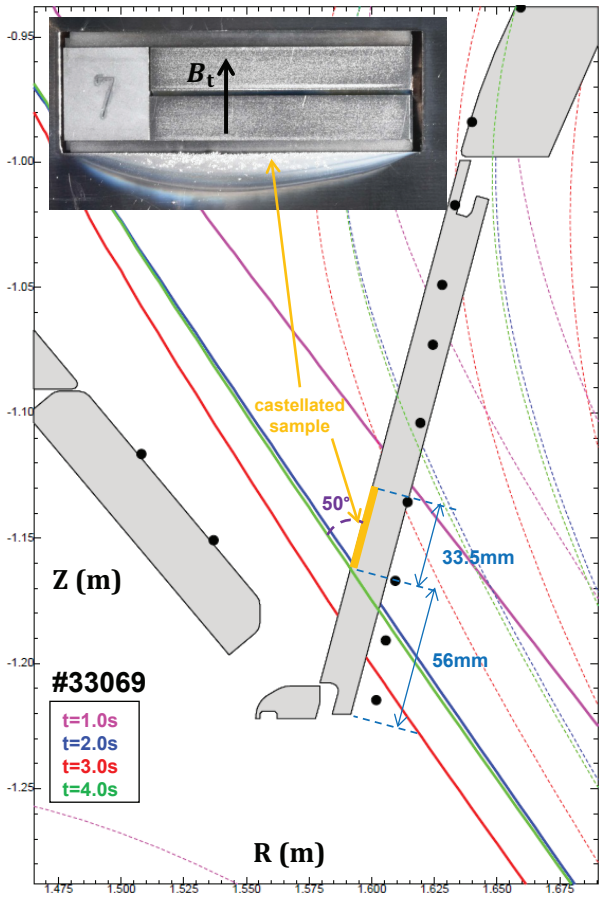

FIG. 3: (Main) Poloidal cross-section of the AUG vessel near the outer divertor target plate where the castellated samples were exposed. The successive flux surface contours of magnetic equilibria reveal the movement of the strike point during the exposure of sample W07 in discharge #33069, where the plasma plateau lasted from 1.26 sec to 4.13 sec. (Insert) View of the W07 castellated structure mounted on sample holder. Surface modifications of the sample holder (due to the melting sustained during the initial heat flux tests) are clearly visible. The toroidal magnetic field is oriented across the gap.

C. Plasma exposures

The scheduled discharges aimed at two incident heat flux regimes; *low power* capable of melting Be proxy dust and *high power* capable of also melting refractory dust. Variations of the exposure time were also targeted, with *short exposures* designed to minimize the ELM incidence (facilitated by swiping the strike point) and *long exposures* limited by the heat capacity of the sample holder.

Initial tests on a dummy dust-free structure (#33067) revealed that the tile covering the sample holder, manufactured from Densimet 185 alloy (W, 2 wt.% Ni, 1 wt.% Fe, supplied by Plansee), had been partially molten due to its strongly reduced thickness close to the sample exposure slot (see also the insert of Fig.3). This imposed rather strong limitations on the energy loads that were realized in all the remaining shots. Overall, ten useful discharges were obtained with variations in the incident heat flux and exposure duration. The H-mode discharge parameters were; toroidal magnetic field $B_t = -2.5\,$T, plasma current $I_p = 0.8\,$MA, power of $2.5 - 5.0\,$MW (neutral beam injection) and 1.9 MW (electron cyclotron resonance heating) for the low and high power exposures, respectively. The line averaged densities were $n_e = (6.3 - 8) \times 10^{19}\,\mathrm{m}^{-3}$.

Due to the lack of direct observations of the castellated samples, the intra-ELM heat fluxes were evaluated from IR camera observations of a neighbouring tile, within the toroidal symmetry assumption. The inter-ELM parameters were deduced from probe measurements and IR camera data. Typical temporal ELM waveforms are illustrated in Fig.4 for the low and high power exposures. The ELM-averaged heat flux $q_\perp$ normal to the monoblock top was $2.6\,\mathrm{MW/m^2}$ and $4.9\,\mathrm{MW/m^2}$, respectively. In all discharges, the magnetic field inclination angle was $\sim 3^\circ$

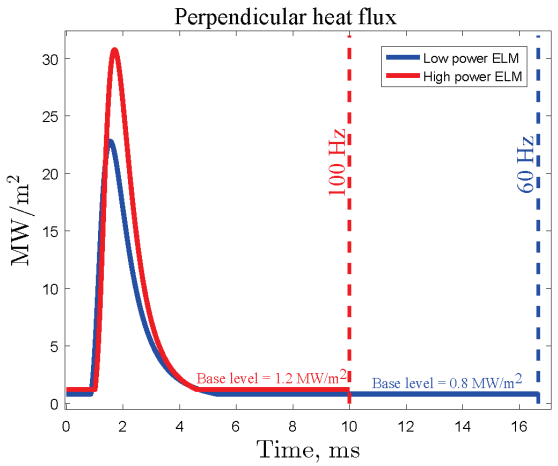

FIG. 4: Characteristic temporal intra-ELM heat flux signals including the inter-ELM base levels and the typical ELM frequencies for the high power exposures (specifically #33077) and low power exposures (specifically #33069), resulting to the time-averaged $q_\perp \simeq 4.9\,\mathrm{MW/m^2}$ and $q_\perp \simeq 2.6\,\mathrm{MW/m^2}$.

with respect to the monoblock top surface tangent.

In discharges dedicated to *long exposures*, the total exposure times were the following: ~ 8 sec low power exposure of W07 in three shots #33068 − 33070, ~ 3 sec high power exposure of W09 in three shots #33074 − 33076, ~ 2 sec high power exposure of W06 in two shots #33077 − 33078. The results of these exposures will be examined in a detailed manner. The outer strike point movement for the long exposures is illustrated in Fig.3.

In discharges dedicated to *short exposures*, namely #33072 (low power exposure of sample W08) and #33073 (high power exposure of sample W10), the outer strike point was promptly swept across the castellated structures during the ramp-up and held above them during the plasma plateau. The post-exposure SEM analysis of the samples revealed no modifications in the dust deposition patterns. This verifies that the modifications taking place during the long exposures can be safely attributed to plasma incidence and that mechanical vibrations or impulsive accelerations of the vessel do not cause remobilization or tangential displacements of the adhered dust grains. These exposures will not be discussed further.

III. EXPERIMENTAL RESULTS

In the castellated samples that were subject to long exposures, the dust spots have undergone various modifications which can be categorized in the following manner: (i) remobilization and tangential displacements, (ii) melting and wetting-induced coagulation, (iii) clustering and cluster re-arrangements. In the *bottom spots*, a very low remobilization activity was observed as well as very few instances of cluster re-arrangements, exemplified in Fig.5. In the *side spots*, few modification instances were observed but the image analysis was hindered by the poor surface quality, thus these spots will not be discussed further. In the *top spots*, directly subject to the plasma heat flux, all aforementioned modifications were present with varying degree. Hence, we shall only analyze the effect of plasma incidence on dust adhered on the top of castellated samples. The results are summarized in Table I.

TABLE I: Summary of the modifications observed in dust deposited on the top spots of the castellated samples after exposure to multiple AUG H-mode discharges. W06 was exposed to an ELM-averaged $q_\perp = 4.9\,\mathrm{MW/m^2}$ for ~ 2 sec, W07 to $q_\perp = 2.6\,\mathrm{MW/m^2}$ for ~ 8 sec, W09 to $q_\perp = 4.9\,\mathrm{MW/m^2}$ for ~ 3 sec. The designation N/A implies that the pre-adhered dust number is too low to allow for reliable particle statistics.

Sample & shot #	Dust & size (μm)	Spot density	Remob. act. (%)	Clustering & melting
W06	W ($5-25$)	moderate	50	Clustering
33077-	W ($\lesssim 1$)	high	low	Clustering
33078	Mo (~ 14)	low	70	None
	Cr ($\lesssim 10$)	high	low	Melting
W07	W ($5-25$)	low	40	Few instances
33068-	W (~ 14)	low	55	None
33070	W ($\lesssim 1$)	high	low	None
	Mo (~ 14)	few grains	N/A	None
	Cu ($\lesssim 5$)	moderate	low	Few instances
	Cr ($\lesssim 10$)	multilayers	high	Coagulation
W09	W ($5-25$)	low	50	None
33074-	W (~ 14)	multilayers	high	Coagulation
33076	W ($\lesssim 1$)	high	low	Clustering
	Mo (~ 14)	low	80	Melting
	Cu ($\lesssim 5$)	high	50	Few instances
	Cr ($\lesssim 10$)	high	low	Melting

Before proceeding, it is worth discussing the strong spatial variations of the incident plasma fluxes as revealed by the different degree of modifications observed in each of the monoblocks of the same castellated sample. The relevant samples are W07 and W09, since they featured top spots on both monoblocks. In W09, the two monoblocks exhibited similar modifications, this is highlighted by the spots with $5-25\,\mu$m W dust which are featured on both monoblocks and are characterized by nearly the same remobilization activity (52% and 47%). On the contrary, in W07, all the spots of one monoblock underwent nearly no modifications whereas remobilization, clustering and even melting was observed in the spots of the adjacent monoblock.

A. Remobilization

Remobilization can be intuitively quantified by the remobilization activity, defined as the number of adhered

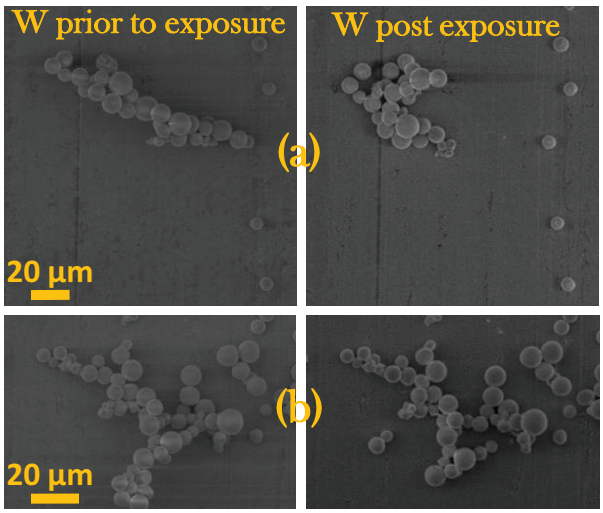

FIG. 5: Zoomed-in SEM images of two $5-25\,\mu$m W bottom spots belonging to sample W09 prior to and post exposure to three H-mode discharges (#33074 – 33076). Two instances of cluster re-arrangements are documented.

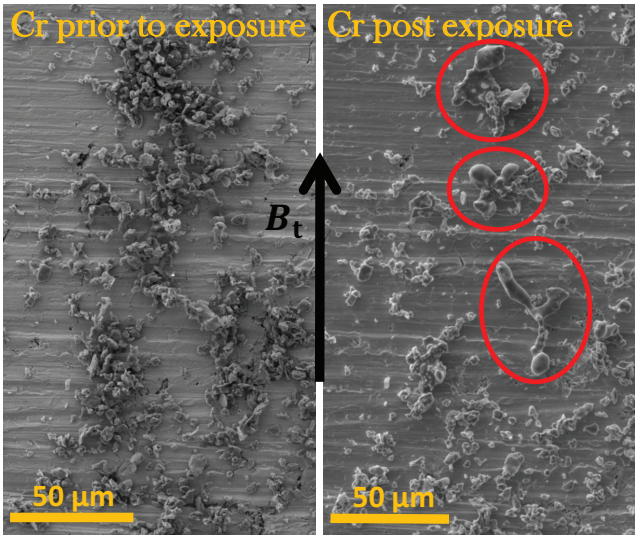

FIG. 6: SEM images of the Cr top spot of sample W07 documenting the phenomenon of wetting induced coagulation. Images prior to and post exposure to three H-mode discharges (#33068 – 33070). Three instances of wetting induced coagulation (marked by red) and multiple instances of cluster melting can be observed. The newly formed dust grains are not spherical most probably owing to the highly irregular shape of the monomers.

dust grains that were removed from the dust spot during plasma exposure over the total number of grains initially adhered on the dust spot [14]. In spite of the fact that the experimental determination of the remobilization activity simply requires particle counting, in many cases only a qualitative assessment is viable. Quantification is impossible for irregular dust shapes, multilayered depositions, intense cluster melting and small dust sizes comparable to the surface roughness length-scale. The remobilization activity for all top spots is provided in Table I.

The adhesive or pull-off force resisting remobilization in the normal direction scales as $\propto R_\mathrm{d}$, whereas plasma-induced forces scale as $\propto R_\mathrm{d}^2$, which clearly implies that larger dust grains should exhibit higher remobilization activities [14, 16]. Despite quantification difficulties and the large inhomogeneity in the ELM-plasma wetting of each dust spot, this expectation is confirmed in Table I, where it can be seen that $14\,\mu$m W and Mo dust exhibit the highest remobilization and $\lesssim 1\,\mu$m W dust exhibits the lowest remobilization. For completeness, it should be pointed out that for multilayers, adhesion can be significantly weaker [14, 16, 17]. The effect of other factors such as non-sphericity, micron and nano-scale roughness as well as impact-induced plasticity has been thoroughly discussed in our previous works [14, 16] and recently confirmed in dedicated measurements of the W-on-W pull-off force with the electrostatic detachment method [26, 27].

Wide optical investigations on the whole top and side monoblock surfaces as well as detailed SEM investigations in the immediate vicinity of the deposited spots were conducted. They revealed that most detached dust must have remobilized away from the castellated samples towards the AUG divertor plasma. The few exceptions where dust was initially detached and then ended up residing back on the substrates will be considered at the end of section III. Therefore, an amount of well-characterized non-intrinsic micron dust (perfectly spherical - high purity W and Mo, high purity Cu and Cr) was essentially injected into AUG. Its identification in future collection activities would provide important information on dust survivability and migration patterns in AUG. However, this is highly unlikely due to not only the limited relative collection area but also the fact that the injected amount is minuscule. A rough estimate was possible for the pure spherical dust populations which resulted to ~ 200 $14\,\mu$m Mo grains, ~ 200 $14\,\mu$m W grains and ~ 1100 $5-25\,\mu$m W grains.

B. Melting and wetting-induced coagulation

The following facts need to be considered for the deeper understanding of melting events [15, 16]; (i) the plasma heat fluxes and exposure times achieved are too modest to cause the melting of isolated adhered dust grains (singlets) of any composition, (ii) the finite thermal contact conductance implies that the number of mediating contacts between the plasma-facing dust grains and the substrate essentially controls the occurrence of melting; in large clusters present in dense and multilayered depositions, heat conduction to the substrate is more inhibited making them more prone to melting, (iii) the inter-ELM period is sufficiently long for the dust grains to cool down to the substrate temperature, but the substrate is not actively cooled and thus its temperature monotonically increases during the exposure, hence longer exposure times

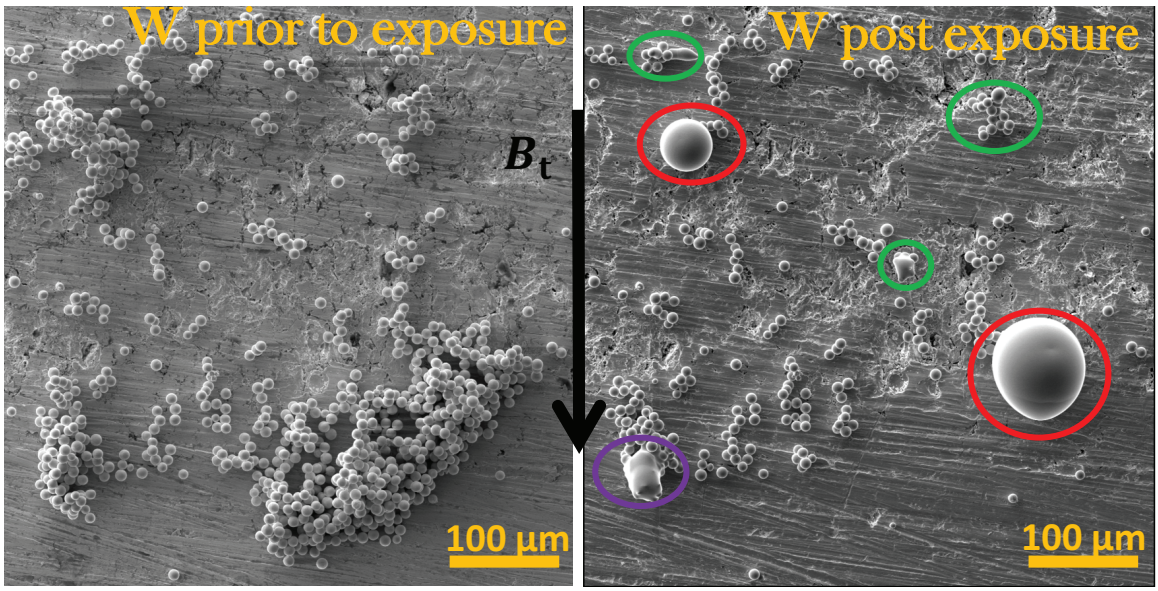

FIG. 7: SEM images of the $\sim 14\,\mu$m W top spot of sample W09 documenting the phenomenon of wetting induced coagulation. Images prior to and post exposure to three H-mode discharges (#33074 – 33076). Three instances of small-scale cluster melting (marked by green), one instance of large-scale cluster melting (purple) and two instances of wetting induced coagulation (red) can be observed. The two newly formed nearly spherical dust grains contain ~ 200 and ~ 50 original grains.

facilitate melting, (iv) cluster melting has a probabilistic character owing to the stochastic nature of roughness which leads to a stochastic thermal contact conductance.

Given the above, melting of isolated dust was never observed while pronounced large-scale melting and the associated phenomenon of wetting-induced coagulation occurred only in the two spots characterized by the highest density of adhered dust and the presence of dust multilayers, see also Table I. In Fig.6, where the Cr deposition is multilayered and rather homogeneous, various instances of cluster melting and wetting-induced coagulation can be observed. The upper dust layer melted and subsequently spread over the bottom dust layers, thus generating elongated larger dust after resolidification [15]. The irregular shape and polydisperse nature of the deposited Cr dust does not allow more quantitative statements. In Fig.7, where the W deposition pattern is strongly inhomogeneous featuring very large clusters, melting led to the generation of very large nearly spherical W dust grains through the mechanism of wetting-induced coagulation. The spherical shape and monodisperse nature of the deposited W dust allows us to estimate that the newly-generated grains contain nearly 200 and 50 dust monomers.

Small-scale melting events have been observed in spots with sparse quantities of adhered W dust, some examples are illustrated in Fig.8. Two W monomers, constituents of a small cluster, have been fused together through their contact area (Fig.8a) and numerous Mo monomers have been fused after one of the top grains melted wetting the remaining ones (Fig.8b). Note that clustering also took place hindering the identification of the original grains.

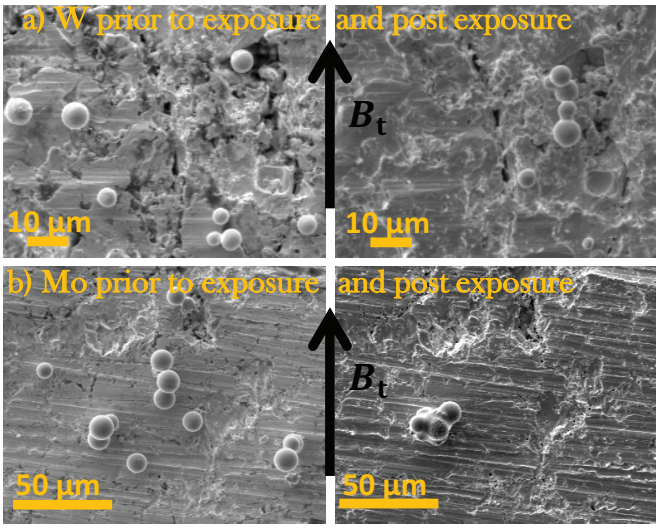

FIG. 8: (a) Zoomed-in SEM images of the $5 - 25\,\mu$m W top spot of sample W07 focusing on an instance of small-scale cluster melting. Images prior to and post exposure to three H-mode discharges (#33068 – 33070); two dust grains part of a cluster have been fused after melting. (b) Zoomed-in SEM images of the Mo top spot of sample W09 focusing on an instance of small-scale cluster melting. Images prior to and post exposure to three H-mode discharges (#33074 – 33076); a newly-formed cluster consisting of approximately $6 - 8$ grains has been fused after melting.

Small-scale melting events have also been observed in spots with sparse quantities of adhered Be-proxy dust, some examples are illustrated in Fig.9.

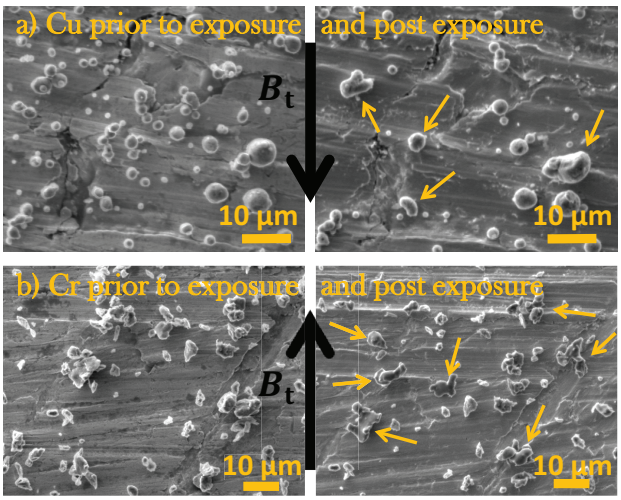

FIG. 9: (a) Zoomed-in SEM images of the Cu top spot of sample W09 focusing on instances of small-scale cluster melting. Images prior to and post exposure to three H-mode discharges (#33074 – 33076); four instances can be discerned as indicated by the arrows. (b) Zoomed-in SEM images of the Cr top spot of sample W06 focusing on instances of small-scale cluster melting. Images prior to and post exposure to two H-mode discharges (#33077 – 33078); seven instances can be discerned as indicated by the arrows. The identification is rather ambiguous owing to the irregular dust shape.

From the SEM images, regardless of the dust composition, it is evident that neither all clusters have an equal remobilization probability nor all the non-detached clusters have undergone melting. The physical processes controlling remobilization and melting are very complex, the main aspects concern the magnitude of the mechanical contact area (dictated by the impact speed and the dust size), the magnitude of the thermal contact conductance (controlled by the surface roughness and dust size), the number of dust monomers constituting the clusters as well as the cluster topology with respect to the incident heat flux (shadowing effect). These aspects will be qualitatively assessed in section IV .

C. Clustering and cluster re-arrangement

Clustering refers to the formation of larger clusters during plasma exposure owing to the mutual approach of isolated grains and/or smaller clusters and their subsequent agglomeration. It has not been possible to discern experimentally whether clustering exclusively occurs through the tangential motion of the adhered dust or it also involves normal motion (*i.e.* temporary remobilization followed by non-local re-attachment). Most probably both mechanisms take place but the former is more frequent, since it has been documented that, for micron sized dust and sub-micron scale roughness, adhesive interactions dominate over frictional interactions [12, 28, 29]. *Cluster re-arrangement* refers to topological changes in adhered

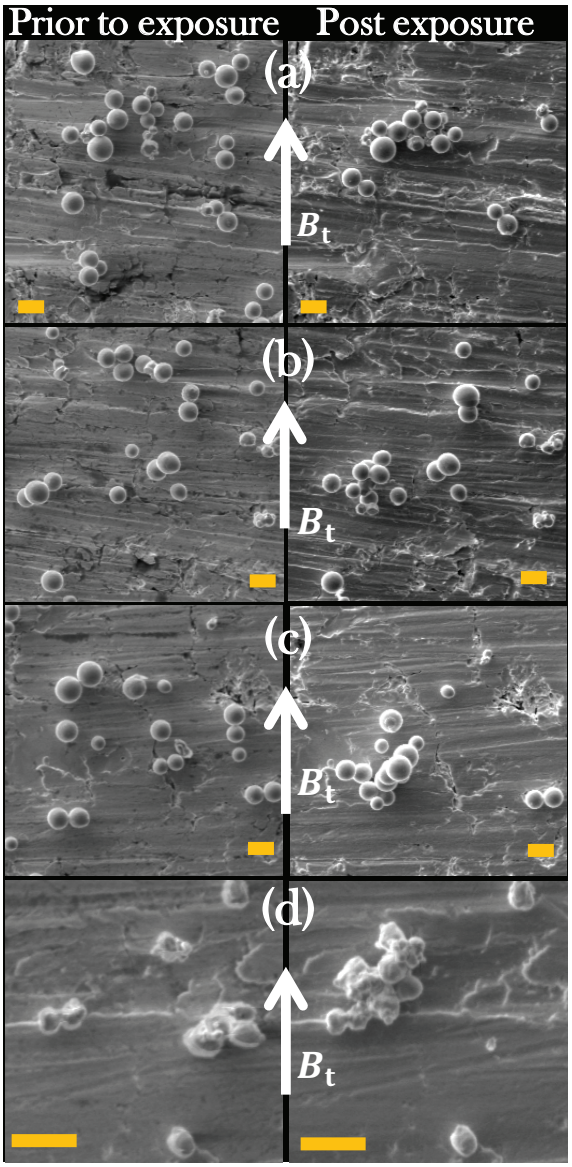

FIG. 10: SEM images documenting the clustering of polydisperse W dust induced by plasma incidence. Zoomed-in images prior to and post exposure with the scale bar corresponding to 10 μm. (a,b) $5-25\,\mu$m spherical W dust adhered to sample W09, (c) $5-25\,\mu$m spherical W dust adhered to sample W06, (d) $\lesssim 1\,\mu$m irregular W dust adhered to sample W06.

clusters during plasma exposure, not necessarily accompanied by the loss or gain of dust monomers. Clustering can have important consequences in view of wetting induced coagulation, whereas cluster re-arrangement is rather inconsequential but is nonetheless indicative of the complexity of momentum exchange between the adhered dust and the incident plasma.

In the first cross-machine studies [14, 15], cluster re-arrangements had taken place after exposures to steady state and transient ELM-like plasmas but no instances of clustering had been observed. However, in more recent experiments with $5-25\,\mu$m W dust in the COMPASS

tokamak, clustering was rather pronounced albeit mainly in L-mode discharges with forced disruptions [16, 17]. In COMPASS, post-mortem observations of arc traces in spot regions characterized by an intense remobilization activity suggested that interaction with arc currents could have played a role [17].

In AUG, various instances of clustering were identified which involved most types of dust populations. The phenomenon is unambiguously observed in spots featuring large dust and characterized by sparse deposition, as illustrated in Fig.10 for the case of polydisperse W dust. In contrast to COMPASS, where the surface roughness was nearly one order of magnitude lower, no arc traces were observed. This does not exclude the occurrence of arcing, since arc traces are hard to detect in the present exposures considering that the expected trace depths [30] are comparable to the top monoblock surface roughness. Given the complexity of the clustering phenomenon, we shall refrain from speculating on the underlying mechanism. We emphasize though that these newly-generated clusters will be more prone to melting during subsequent exposures, thus clustering promotes wetting-induced coagulation and the generation of large dust.

D. Droplet impacts of remobilized refractory dust

As aforementioned, most detached dust was injected into the AUG plasma and only few detached grains ended up residing back on the castellated substrate. This was concluded from detailed optical and SEM analysis but not from camera observations. Resolving the individual trajectories of remobilized dust is impossible given the low spatial resolution, the small sizes and the fact that every spot is incandescent [28]. Nevertheless, detached dust (even Mo and W) promptly melts in the ELMy divertor plasma. Consequently, in case of droplet incidence back on the substrate, there is a high chance that it adheres locally. Signatures of droplet impact as well as the possible large distance of the sticking site from the deposition spots suffice to distinguish these incidents from simple tangential displacements of adhered dust. As we shall examine, the morphology of the resolidified droplets allows the identification of the impact velocity direction. More important, knowledge of dust composition in the neighboring spots allows tracking of the origin of the droplet.

Due to the small acceleration lengths and the large mass densities of the refractory dust, droplet splashing should not be possible [31]. It is instructive to first consider some elementary physics of droplet impact in this rebound regime. At the initial stage of the impact, most of the incident kinetic energy is expended into the flattening of the droplet. Surface tension is able to restrict the inertial spreading of the external layers, while the inner layers begin to recoil under the action of the contact forces. This backward flow is always counteracted by cohesion. In the present scenario, the large $\sim 2000\,\mathrm{K}$ temperature difference between the droplet and the substrate implies that resolidification as well as the increase of viscosity will also counteract recoiling. As a result, a characteristic "fried-egg" morphology emerges for near-normal impacts, a characteristic "cometary-tail" morphology along the tangential impact velocity direction emerges for near-tangential impacts and an intermediate morphology emerges for oblique impacts [32, 33].

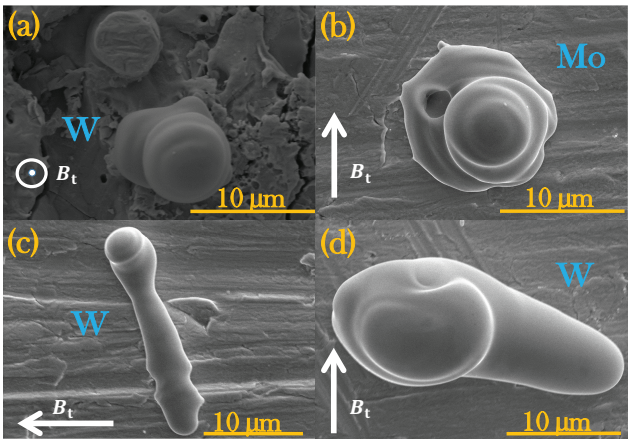

FIG. 11: Instances of droplet impacts of remobilized refractory dust; near-normal (W in a, Mo in b), near-tangential (W in c) and oblique (W in d). The morphology of the resolidified droplets is distinctly different from the morphology of clusters that have undergone wetting-induced coagulation. (a) Resolidified W dust detected on the side surface of the C monoblock of W07, 70 μm below the Mo spot. Two W spots were deposited on the same monoblock, but there was absolutely no remobilization in these spots. The grain must have originated from the opposite A monoblock and most probably from the exactly opposite spot that contains $5-25\,\mu$m W dust, where 40% remobilization was observed. (b) Resolidified Mo dust detected on the top monoblock surface of W06 exactly between the Mo and the 1 μm W spots, 2 mm from the Mo spot. The grain must have originated from the neighboring spot, which is the only one with Mo dust and where 70% remobilization occurred. (c,d) Resolidified W dust detected on the top monoblock surface of W06 between the $5-25\,\mu$m W and Mo spots. These two grains must have originated from the neighboring spot, where 50% remobilization occurred.

Few tens of such droplet impacts of remobilized refractory (W, Mo) dust were detected. In case of tungsten dust, the composition was $> 99\,$wt.% W implying that it most probably did not originate from the PFCs or the Densimet alloy holder. The most characteristic instances have been depicted in Fig.11. In the first example, the W droplet normally impacted on the monoblock side and must have remobilized from the opposite monoblock top. In the second example, the Mo droplet normally impacted on the monoblock top and must have remobilized from the neighboring spot. In the last two examples, the W droplets obliquely impacted on the monoblock top and must have originated from the neighboring spot; the tangential velocity direction is different which is indicative of the complexity of the interaction of the remobilized dust grains with the near-sheath ELM plasma [28, 34].

IV. HEAT TRANSFER SIMULATIONS

A. Implementation and theoretical input

The 3D FEM heat conduction solver has been implemented in COMSOL Multiphysics [16, 35]. A schematic of the deposition of the plasma heat flux on the substrate and the dust grains is illustrated in Fig.12, where the angle $\chi \simeq 3^\circ$ between the magnetic field lines and the substrate tangent as well as the angle ϕ between the collinear dust centers and the substrate normal are defined. Cluster arrangements with varying numbers of monomers and asymmetry angles will be investigated. The time dependent field-line parallel heat flux has been calculated from the temporal intra-ELM and inter-ELM waveforms plotted in Fig.4. The heat flux shadowing has been assumed to follow the optical approximation for both the substrate and the dust grains.

The **cooling** of dust takes place mainly through heat conduction across the dust-dust and dust-substrate contacts, thermionic emission, vaporization and thermal radiation. The expenditure of the latent heat of fusion during the solid-liquid phase transition was accounted for. In the modelling of *thermionic emission*, the polycrystalline work-functions $W_\mathrm{f}(\mathrm{W}) = 4.55\,\mathrm{eV}$, $W_\mathrm{f}(\mathrm{Cu}) = 4.60\,\mathrm{eV}$, $W_\mathrm{f}(\mathrm{Cr}) = 4.5\,\mathrm{eV}$ [36] as well as the Richardson constants $A_\mathrm{R}(\mathrm{W}) = 60\,\mathrm{Acm^{-2}K^{-2}}$, $A_\mathrm{R}(\mathrm{Cu}) = 80\,\mathrm{Acm^{-2}K^{-2}}$, $A_\mathrm{R}(\mathrm{Cr}) = 55\,\mathrm{Acm^{-2}K^{-2}}$ [37] were employed. For simplicity, thermionic emission was assumed to be unimpeded by space-charge effects and re-deposition by Larmor gyration [38, 39]. Thermionic cooling was mostly important for W, since for Cu and Cr the onset of intense vaporization did not allow the temperature to exceed $\sim 2600\,\mathrm{K}$ and $\sim 2500\,\mathrm{K}$, respectively. In the modelling of *vaporization*, the atomic flux leaving the dust surface was estimated with the Hertz-Knudsen formula [12]. The temperature dependence of the vapor pressure was considered following experimental results [40]. As expected, vaporization was ineffective below the melting point. In the modelling of *thermal radiation*, both the temperature and the size dependence of the spectral emissivity were taken into account. The analytical Mie theory for homogeneous spherical objects was employed. For temperatures close to or exceeding the W melting point, radiative cooling becomes negligible compared to the other cooling channels.

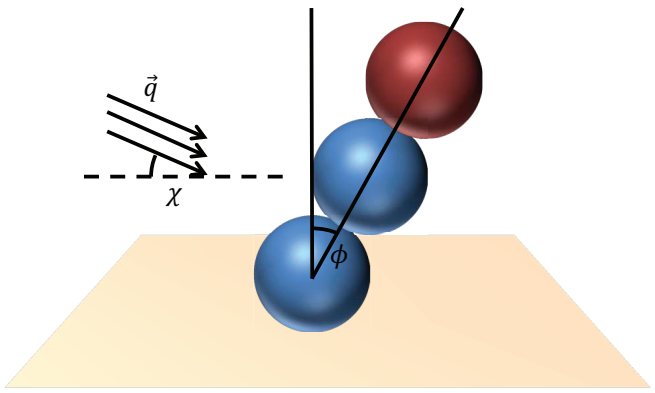

FIG. 12: Sketch of dust configuration inside the cluster, definition of the cluster asymmetry angle ϕ and the plasma incident angle χ with respect to the substrate surface. For the sake of simplicity, coplanarity is assumed.

The dust-substrate and dust-dust **contact radii** have been calculated following analytical models of elastic-perfectly plastic adhesive impacts [12, 15]. In these calculations, the effects of the deposition method and the cluster formation mechanism have been taken into account [35] with the impact speed set equal to the dust carrier speed for the dust-substrate computations (application of the Thornton and Ning model [41]) and set equal to zero for the dust-dust computations (application of the Johnson-Kendall-Roberts theory [42] for zero load). For the evaluations, numerous mechanical properties are necessary; the Young's modulus E, the Poisson's ratio ν, the yield strength γ_y and the surface energy Γ. The size-dependence of the yield strength has been considered in a manner analogous to Hall-Petch grain-boundary strengthening, *i.e.* $\gamma_\mathrm{y} = \gamma_\mathrm{b} + k_\mathrm{y}/\sqrt{d_\mathrm{grain}}$, where γ_b is the bulk yield strength and k_y the strengthening parameter. The room-temperature values of the above properties that have been employed for Cu and Cr are listed in Table II. The employed material properties for W are as specified in Table I of Ref.[12].

The previous implementation of **heat flow constriction** [16] consisted of different analytical expressions depending on the mode of deformation, elastic [49] or plastic [50], with the latter concluded to be appropriate for dust-in-fusion applications. The description has been updated in order to account for plastic flow due to the interaction between individual asperities. The thermal contact conductance is now modelled by the expression [51]

$$h_\mathrm{c} = 1.25\,\frac{k_\mathrm{eff}\tan\theta}{\sigma}\left(\frac{P}{P+H}\right)^{0.95}, \qquad (1)$$

In the above: k_eff is the effective thermal conductivity defined by $k_\mathrm{eff} = 2k_1k_2/(k_1+k_2)$ since the thermal resistances of the two contacting bodies (labelled by 1,2) operate in series, $\tan\theta$ is the effective mean value of the absolute asperity slope given by $\tan\theta = \sqrt{\tan^2\theta_1 + \tan^2\theta_2}$, σ is the effective standard deviation of the asperity height given by $\sigma = \sqrt{\sigma_1^2+\sigma_2^2}$, H is the micro-hardness of the softer contacting body and P is the externally applied pressure. The correlation $P/(P+H)$ represents the relative area in contact and accounts for plastic work during compression [52]. The external pressure, in absence of sheath models including adhered dust, is assumed to be equal to the average positive part of the JKR stress-profile [42] across the circular contact [35]. The surface roughness characteristics of the substrate at the nanometer scale of the contact have been measured with atomic force microscopy (AFM), which yielded $\sigma = 21.2\,\mathrm{nm}$ and $\tan\theta = 0.28$. The same values were employed for the

TABLE II: Room temperature mechanical properties for Cu, Cr and Be. The respective melting points are 1358 K, 2180 K and 1560 K. The bulk yield strength of Cr varies between literature sources [47, 48] and manufacturers, thus two extreme values have been employed (producing error bars in the simulations). The proximity between the mechanical properties of Cr and Be is evident.

	E [GPa]	ν	γ_b [MPa]	k_y [MPa μm$^{1/2}$]	H_b [MPa]	Γ [J/m^2]
Cu	126	0.33 [43]	92	399 [44]	369 [45]	1.59 [46]
Cr	286	0.21 [43]	122-400	898 [47]	1060 [45]	2.03 [46]
Be	297	0.05 [43]	395	410 [44]	1120 [45]	1.83 [46]

roughness characteristics of the dust surfaces, for which AFM measurements could not be performed. The size-dependent hardness, $H = H_b + k_H/\sqrt{d_{grain}}$, has been determined by assuming that the ratio H/γ_y is constant for all dust sizes [53, 54]. This clearly implies that $k_H/k_y = H_b/\gamma_b$ and allows the computation of the unknown k_H with the aid of Table II. We stress that overall heat flow constriction is caused by the finite dust-substrate or dust-dust contact areas (microscopic effect) as well as the presence of surface roughness (nanoscopic effect). The implementation of thermal contact conductance captures the latter effect.

In order to illustrate the central role of the finite value of the thermal contact conductance, the heuristic limits $h_c \to \infty$ and $h_c \to 0$ will also be considered in all simulated scenarios. These limits correspond to perfect thermal contact (where microscopic but not nanoscopic heat flow constriction is taken into account) and thermal insulation, respectively [16]. We point out that the adopted values for σ, θ exhibit variations along the substrate, which implies that the thermal contact conductance has a probabilistic character. In view of Eq.(1), it becomes apparent that, due to nano-roughness, the occurrence of cluster melting and wetting-induced coagulation should be of stochastic nature, as clearly observed in the present experiments.

Finally, we note that it is implicitly assumed that the state of the contact is time-independent and fully established during dust deposition. Since the contact area depends on various mechanical properties, this implies that room-temperature values need to be employed for these quantities. On the other hand, the temperature dependence of thermophysical properties (mass density, thermal conductivity, specific heat capacity) has been considered. In the case of tungsten, the recommendations of Ref.[55] have been followed.

B. Numerical results

Earlier heat transfer simulations [15, 16] had managed to reproduce the main experimental results also observed in the AUG experiments; the fact that clusters can melt under much lower heat loads than bulk materials or isolated dust grains owing to the imperfect thermal contact [15] and the fact that cluster melting has a strong statistical character owing to the dependence of the thermal contact conductance on the local surface roughness characteristics [16]. Here we shall explore some other dependencies.

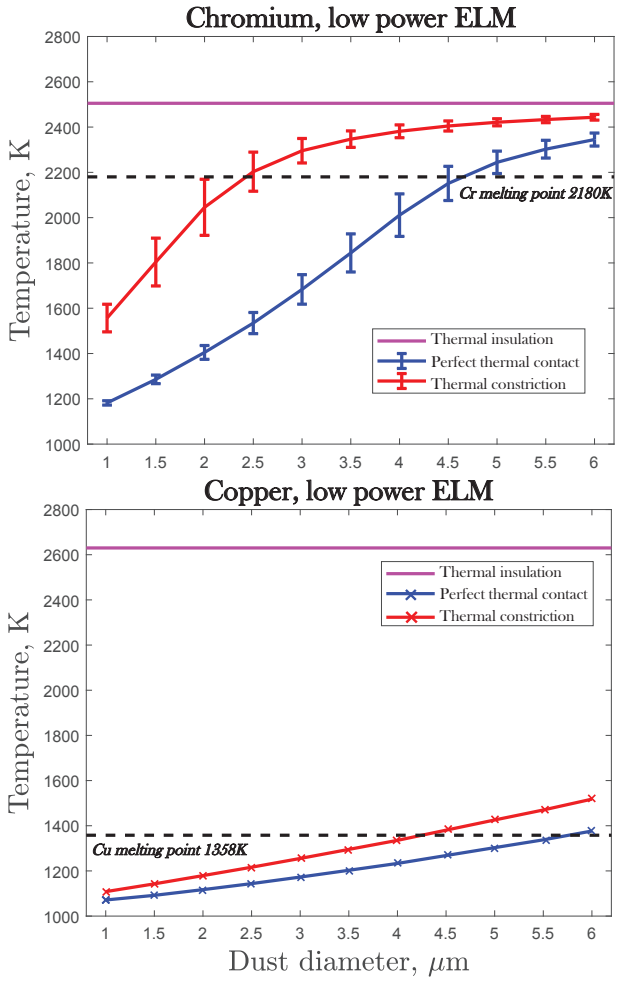

FIG. 13: Interaction of adhered Be-proxy dust grains with the final ELM of a low power AUG exposure. The maximum temperature attained by the upper dust grain in a cluster of two Cr (upper figure) or Cu (lower figure) dust monomers during interaction with the final ELM of a low power discharge. The doublet is placed axi-symmetrically with respect to the surface normal, $\phi = 0°$ (see Fig.12 for the definition of the angle). The dust monomers are spherical, of the same composition and of equal size. Results are shown for varying dust diameters. The simulated diameters vary from $1 - 6\,\mu$m with a step of $0.5\,\mu$m. The error bars in the case of Cr correspond to the lower and upper values of the yield strength encountered in the literature (see Table II and its caption).

In spite of the imperfect thermal contact, the average ELM frequency (60 Hz) is sufficiently low to ensure that the dust temperature relaxes close to the substrate temperature within the inter-ELM period [35]. In particular, after the impact of the heat flux maximum *i.e.* during the

falling edge of the ELM pulse, the dust temperatures are so elevated that the total cooling flux (thermionic emission, vaporization, thermal radiation) and the Fourier conduction flux greatly exceed the incident plasma heat flux resulting to a decrease of the dust temperature. Even when accounting for heat constriction, the decay is rapid owing to the small heat capacity of the micron-sized dust. In addition, due to the lack of active cooling, the substrate temperature does not acquire a steady-state value but monotonically increases during the exposures. As a consequence, it suffices to perform simulations of the final intra-ELM period and employ a homogeneous substrate and dust temperature of 1000 K as initial condition. Simulations of the low power exposures were performed with the temporal heat flux adopted from Fig.4 (blue curve). Spatial variations were neglected being insignificant at the scale of the dust grains.

1. *Beryllium proxy dust*

As discerned from Table I, Cr clusters exhibit a stronger melting tendency than Cu clusters, in spite of $T_{\rm m}({\rm Cu}) = 1358\,{\rm K}$ and $T_{\rm m}({\rm Cr}) = 2180\,{\rm K}$. This should not be solely attributed to differences in the deposition pattern (high density spots were available for both populations) or to differences in the dust sizes (the actual size distributions were similar). Furthermore, the irregular flaky Cr shape should lead to larger contact areas and stronger conduction to the substrate compared to spheroidal shapes, thus decreasing the Cr cluster melting tendency. Fig.13 shows simulation results of the interaction of Cr and Cu clusters with the ELM heat pulse. The simulated clusters consist of two identical spherical dust monomers and are placed axisymmetrically with respect to the surface normal ($\phi = 0°$). The maximum temperature attained by the upper monomer is plotted for the Cr and Cu doublets (upper and lower panel, respectively) as a function of the dust size. Results for finite contact conductances, perfect thermal contact and thermal insulation are provided.

Within the size ranges of interest, the *thermal insulation* results are nearly independent of the dust diameter. In the absence of conduction, the heat capacity is low enough so that the energy deposited by one ELM suffices for the grains to reach the equilibrium temperature at which the incident plasma heat flux is balanced by the dust cooling channels (predominantly vaporization). This occurs at the same temperature for dust of the same composition, because of the surface nature of both plasma collection and emission cooling. In addition, for both Cu and Cr, these equilibrium temperatures are very close. Concerning vaporization, the relevant latent heat and the normal boiling points of both materials are very close, the latter implies that the vapor pressures at elevated temperatures are also similar. On the other hand, the *perfect thermal contact* results strongly depend on the dust size, primarily due to the proportionality of the contact area to the dust diameter.

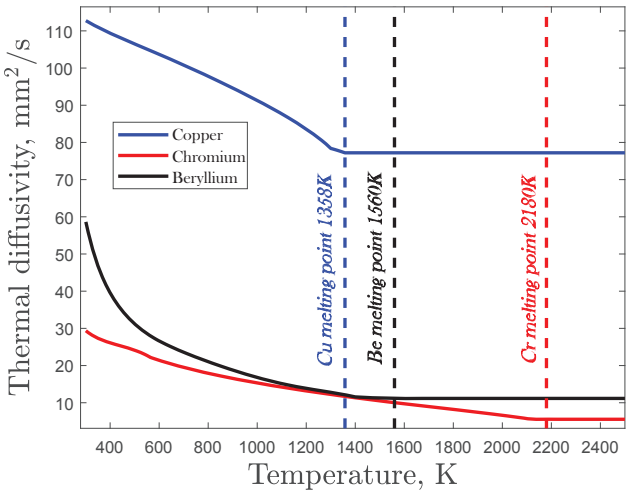

FIG. 14: The temperature dependent chromium and copper thermal diffusivities as employed in the simulations. The dashed lines indicate the respective melting points. The thermal diffusivity of beryllium has also been plotted for comparison: Cr and Be have similar diffusivities at elevated temperatures, whereas Cu and Be only have similar melting points. The relevant thermophysical properties (mass density, specific heat capacity, thermal conductivity) have been adopted from Refs.[59–61].

The *finite thermal contact conductance* simulations reveal a rather similar melting tendency between equally sized Cu and Cr doublets, in spite of the significant melting point differences. In fact, Cr doublets are somewhat more prone to melting, with the maximum temperature curve crossing the melting point for smaller sizes. For both materials, it is evident that the inclusion of thermal constriction significantly reduces the minimum dust size where melting can occur. In the case of Cu doublets, the results are very close to the perfect thermal contact limit and far from the thermal insulation limit. On the other hand, in the case of Cr doublets, the results are close to the perfect thermal contact limit for small sizes and close to the thermal insulation limit for large sizes. These results can be explained by the much higher Cu thermal diffusivity (factor of $\sim 5-15$ larger than Cr, with the ratio depending on the temperature see Fig.14) as well as the nearly double dust-substrate and dust-dust contact radii of Cu. The latter fact implies that, for the same dust size, Cu has weaker constriction (scaling inversely with the contact radius). Overall, heat can easier diffuse through Cu dust but also larger surface boundaries are available for its propagation. Hence, heat exchange with the neighbouring grain and the underlying substrate is much more efficient, eventually enabling Cu to withstand larger heat fluxes than Cr dust prior to melting.

It is worth pointing out that the temperatures attained by adhered dust in the case of thermal insulation are close to the temperatures attained by dust that has remobilized in the plasma. These temperatures are not exactly the same due to the different sheath heat transmission

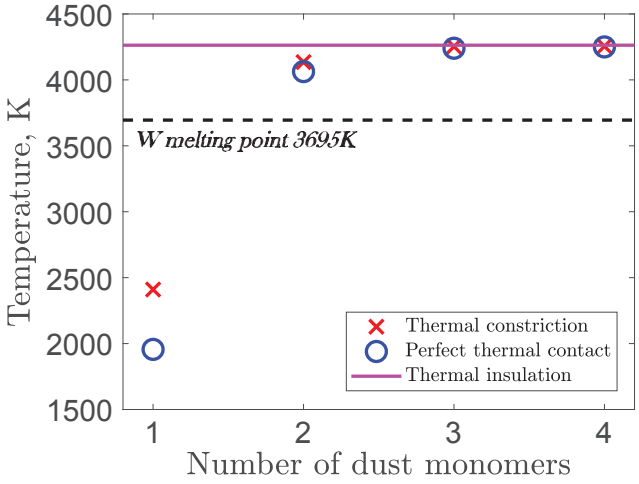

FIG. 15: Interaction of adhered W dust grains with the final ELM of a low power AUG exposure. The maximum temperature attained by the top dust grain in axisymmetric clusters consisting of identical spherical W monomers of 15 μm diameter. Results are shown for varying number of monomers.

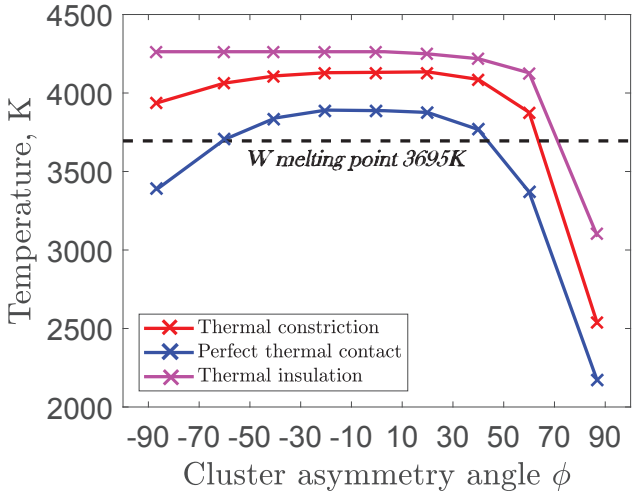

FIG. 16: Interaction of adhered W dust grains with the final ELM of a low power AUG exposure. The maximum temperature attained by the top dust grain in non-axisymmetric doublets consisting of identical spherical W monomers of 15 μm diameter. Results are shown for varying values of the cluster asymmetry angle ϕ, previously defined in Fig.12. The simulated asymmetry angles are $\phi = \pm 87°, \pm 60°, \pm 40°, \pm 20°, 0°$. The extrema revealed in the case of downstream ($\phi = 3°$) and upstream ($\phi = -87°$) cluster placement are extensively discussed in the main text.

coefficients involved (thin versus thick sheath) and the fact that the remobilized dust is floating. The thermal insulation temperatures are very close to the normal boiling points of Cr and Cu, which implies that remobilized Cr or Cu dust will promptly vaporize and rapidly shrink in size during interaction with the ELM. This explains why droplet impacts were only observed for remobilized refractory dust but not for remobilized Be-proxy dust.

2. *Tungsten dust*

The emergence of thermally insulated behavior for large clusters constitutes the basis of wetting induced coagulation. The gradual transition to insulation will be studied by varying the number of monomers in axisymmetric clusters consisting of 15 μm W monomers. In Fig.15, the maximum temperature of the top grain is illustrated for isolated dust, doublets, triplets, quartets. It is clear that, already for triplets, the cluster is essentially thermally insulated. The thermal insulation, finite thermal contact conductance and perfect thermal contact curves overlap because the purely geometrical (microscopic) heat flow constriction for the uppermost grain is very strong. This is a multiplicative effect; the numerous mediating small contact areas gradually diminish local temperature gradients making heat conduction negligible.

Finally, we shall explore the effect of different cluster orientations with respect to the magnetic field inclination which coincides with the heat flux incidence within the optical approximation. In Fig.16, the maximum temperature of the top grain is illustrated for non-axisymmetric doublets consisting of 15 μm W monomers. The *thermal insulation* curve has a shape dictated solely by the heat flux shadowing of the top dust grain. It is constant within the interval from $\phi = -87°$ up to $\phi = 3°$, where a hemispherical surface is always subject to the heat flux. It becomes monotonically decreasing from $\phi = 3°$, since the top grain becomes increasingly shadowed by the bottom grain. The *perfect and finite thermal contact conductance* curves are qualitatively the same, their shape is dictated by the relative heat flux shadowing between the top and the bottom grain. These curves exhibit a local minimum for $\phi = -87°$. At this angle, the bottom grain is entirely shadowed from the incident heat flux, whereas the top grain hemisphere is subject to the heat flux. Compared to slightly smaller or larger angles, stronger temperature gradients are initially formed near the contact area that lead to strong heat conduction away from the top grain thus reducing its maximum temperature. The curves become monotonically increasing from $\phi = -87°$ up to $\phi = 3°$. At this interval, a hemisphere of the top grain is constantly exposed to the heat flux and an increasing surface of the bottom grain becomes gradually unshielded. As a consequence, heat conduction from the top grain becomes more inhibited leading to higher maximum temperatures. The curves become monotonically decreasing from $\phi = 3°$. This stems from the fact that the bottom grain hemisphere is now constantly subject to the heat flux and the top grain becomes increasingly shadowed. We point out that, during ELM incidence, the ion Larmor radii are comparable to the considered dust sizes (even the electron Larmor radii are not negligible). Finite Larmor effects should smoothen geometrical heat flux shadowing and thus also the computed curves.

V. DISCUSSION AND CONCLUSIONS

Castellated W substrates with pre-adhered micron dust were exposed to ELMy H-mode discharges in the divertor of ASDEX-Upgrade in order to investigate the interaction of adhered dust with transient heat loads and to address whether gaps constitute a dust accumulation site. Refractory metal dust (W, Mo) and Be proxy dust (Cu, Cr) was deposited in a controlled manner at predefined spots located on the top and side monoblock surfaces as well as on the gap bottom. Five substrates were exposed in ten discharges to normal ELM-averaged heat fluxes of $2.6\,\mathrm{MW/m^2}$ and $4.9\,\mathrm{MW/m^2}$, the exposure times were up to 8 s for the low power pulses and up to 3 s for the high power pulses. Detailed SEM mapping of the spots prior to and after the exposures allowed the identification of instances of dust remobilization, tangential displacements, clustering as well as melting and wetting-induced coagulation. The large number of dust spots combined with the different exposure scenarios provided a sound statistical basis for the estimation of the remobilization activity as well as the clustering and melting occurrence.

Conclusions concerning dust deposited on the top surface of the monoblocks and, thus, directly subject to the plasma heat flux (statistics from 20 spots); **(i)** In accordance to theoretical expectations and previous experiments [14–19], the remobilization activity was higher for larger grains and dust clusters. As a consequence, the remobilization activity mainly depended on the dust size and spot density while no systematic dependencies on the morphology and composition were observed. **(ii)** Cluster melting and wetting-induced coagulation were observed not only for W dust but also for Mo, Cr and Cu dust. Melting of isolated dust grains was never observed. The interaction of the adhered dust clusters with the ELM heat flux appeared to be qualitatively the same, regardless of the dust composition. The latter observation should not be generalized. Due to the modest ELM heat fluxes achieved, droplet spreading and atomic interdiffusion phenomena (which have a strong chemical character) should have been limited. **(iii)** Clustering was identified to take place for most dust populations. Clustering was previously observed in COMPASS but not in Pilot-PSI. It is possible that the inclined magnetic field topology facilitates tangential displacements (easier to be realized because friction is weaker than adhesion) which ultimately lead to clustering. **(iv)** Overall, the present observations are consistent with previous experiments carried out in DIII-D, COMPASS and Pilot-PSI with W dust adhered to planar W samples [14–16].

Conclusions concerning dust deposited on the side surface of the monoblocks (statistics from 4 spots) and the bottom surface of the gaps (statistics from 12 spots); **(i)** The side spots are magnetically shadowed from the incident plasma and, hence, receive much less heat flux (none within the optical approximation) [56]. In spite of the limited statistics and the poor surface quality, the observation of few post-exposure modifications is consistent with such a restricted interaction with the plasma. **(ii)** The bottom spots can only interact with parasitic plasmas generated from the neutrals present inside the gap by direct photo-ionization and/or electron impact ionization by surface photo-electrons [57, 58]. These cold tenuous plasmas are unable to cause any modifications to the adhered dust, as demonstrated by the results of the post-exposure SEM analysis. The weakness of the plasma-induced forces inside the gap is highlighted by the fact that 6 of the 12 bottom spots contained high density multi-layered dust that is characterized by significantly weaker adhesion. **(iii)** Due to the placement of the top spots in the immediate vicinity of the gap (see Fig.2b) as well as the respectable overall remobilization activity observed in the top spots (see Table I), it is possible that many of the detached dust grains ended up residing on the side surface of the monoblocks. This could occur in the case of either mainly tangential dust motion or mainly normal dust motion in the presence of attractive electrostatic fields in the gap. Such a preferential dust accumulation was not observed, see also Ref.[28]. However, it should be mentioned that the poor quality of the side surfaces did not allow for a detailed SEM analysis. **(iv)** Overall, we conclude that, even though the castellations (bottom and side surfaces) can efficiently trap locally adhered dust, they do not constitute dust accumulation sites due to the facts that the monoblock plasma-wetted area is much larger than the gap entrance area and that the majority of the locally remobilized dust does not move towards the gap.

Three-dimensional finite-element modelling of the energy transfer between the incident plasma and the adhered dust was performed based on the optical approximation. The simulations focused on identifying the onset of cluster melting. Apart from the standard cooling channels, heat flow constriction due to the finite dust-substrate and dust-dust contact areas (microscopic effect) and the presence of surface roughness (nanoscopic effect) was considered. Our previous heat transfer simulations had managed to reproduce the experimental fact that clusters can melt under much lower heat loads than bulk materials or isolated dust grains as well as the observed statistical nature of cluster melting [15, 16]. Here, a parametric study of the basic dependencies on the dust size, dust composition, monomer number and cluster topology was conducted. FEM modelling successfully reproduced the slightly stronger melting tendency observed for Cr clusters compared to Cu clusters as well as the increasing melting tendency for larger clusters due to the transition to thermally insulated behavior as the number of the constituent monomers increases.

We re-iterate that sample holder safety considerations imposed limitations on the time-averaged transient heat fluxes that were realized in these experiments. Exposures at higher intra-ELM heat fluxes are necessary for reliable extrapolations to ITER concerning the survivability of Be dust on hot W surfaces. For higher heat fluxes, the adhered grains will remain transiently molten for longer

times allowing for droplet spreading and atomic interdiffusion to determine the macro-morphological changes the dust-substrate system will be subject to.

Acknowledgments

This work has been carried out within the framework of the EUROfusion Consortium and has received funding from the Euratom research and training programme 2014-2018 under grant agreement No 633053. Work performed under EUROfusion WP MST1, WP-PFC. The views and opinions expressed herein do not necessarily reflect those of the European Commission.

[1] Roth J. *et al.* 2009 *J. Nucl. Mater.* **390391** 1
[2] Shimada M. *et al.* 2013 *J. Nucl. Mater.* **438** S996
[3] Taylor N., Alejaldre C. and Cortes P. 2013 *Fusion Sci. Technol.* **64** 111
[4] Sharpe J. P., Petti D. A. and Bartels H.-W. 2002 *Fusion Eng. Des.* **63-64** 153
[5] Garkusha I. E. *et al.* 2009 *Phys. Scr.* **T138** 014054
[6] Makhlaj V. A. *et al.* 2014 *Phys. Scr.* **T159** 014024
[7] Kupriyanov I. B. *et al.* 2015 *J. Nucl. Mater.* **463** 781
[8] Kovalenko D. V. *et al.* 2017 *Nucl. Mater. Energy* **12** 156
[9] Pestchanyi S., Garkusha I., Makhlaj V. and Landman I. 2011 *Phys. Scr.* **T145** 014062
[10] Bazylev B. *et al.* 2011 *J. Nucl. Mater.* **417** 655
[11] Krasheninnikov S. I., Smirnov R. D. and Rudakov D. L. 2011 *Plasma Phys. Control. Fusion* **53** 083001
[12] Vignitchouk L., Tolias P. and Ratynskaia S. 2014 *Plasma Phys. Control. Fusion* **56** 095005
[13] Ratynskaia S. *et al.* 2013 *Nucl. Fusion* **53** 123002
[14] Tolias P. *et al.* 2016 *Plasma Phys. Control. Fusion* **58** 025009
[15] Ratynskaia S. *et al.* 2017 *Nucl. Fusion* **56** 066010
[16] Ratynskaia S. *et al.* 2017 *Nucl. Mater. Energy* **12** 569
[17] Weinzettl V. *et al.* 2017 *Fusion Eng. Des.* **124** 446
[18] Bykov I. *et al.* 2017 *Nucl. Mater. Energy* **12** 379
[19] De Angeli M. *et al.* 2017 *Nucl. Mater. Energy* **12** 536
[20] Herrmann A. *et al.* 2015 *Nucl. Fusion* **55** 063015
[21] Rohde V. *et al.* 2009 *Phys. Scr.* **T138** 014024
[22] Endstrasser N. *et al.* 2011 *Phys. Scr.* **T145** 014021
[23] Balden M. *et al.* 2014 *Nucl. Fusion* **54** 073010
[24] Endstrasser N. *et al.* 2011 *J. Nucl. Mater.* **415** S1085
[25] Brochard F. *et al.* 2017 *Nucl. Fusion* **57** 036002
[26] Riva G. *et al.* 2017 *Nucl. Mater. Energy* **12** 593
[27] Tolias P. *et al.* 2018 *Nucl. Mater. Energy* (submitted)
[28] Shalpegin A. *et al.* 2015 *Nucl. Fusion* **55** 112001
[29] Tolias P. *et al.* 2017 *Nucl. Mater. Energy* **12** 524
[30] Rohde V. *et al.* 2016 *Nucl. Mater. Energy* **9** 36
[31] Yarin A. L. 2006 *Annu. Rev. Fluid Mech.* **38** 159
[32] Aziz S. D. and Chandra S. 2000 *Int. J. Heat Mass Transfer* **43** 2841
[33] Pasandideh-Fard M., Chandra S. and Mostaghimi J. 2002 *Int. J. Heat Mass Transfer* **45** 2229
[34] Delzanno G. L. and Tang X. 2014 *Phys. Plasmas* **21** 022502
[35] Thorén E. 2016 MSc Thesis *Heating of Adhered Metallic Dust in Tokamaks* (Luleå University of Technology: Luleå)
[36] Michaelson H. B. 1977 *J. Appl. Phys.* **48** 4729
[37] Fomenko V. S. 1966 *Handbook of Thermionic Properties* (Plenum: New York)
[38] Komm M. *et al.* 2017 *Plasma Phys. Control. Fusion* **59** 094002
[39] Komm M. *et al.* 2017 *Phys. Scr.* **T170** 014069
[40] Stull D. 1947 *Ind. Eng. Chem.* **39** 540
[41] Thornton C. and Ning Z. 1998 *Powder Technol.* **99** 154
[42] Johnson K. L., Kendall K. and Roberts A. D. 1971 *Proc. Royal Soc. A* **324** 301
[43] Simon N. J., Drexler E. S. and Reed R. P. 1992 *Natl. Inst. Stand. Technol. Mono.* **177**; Street R. 1963 *Phys. Rev. Lett.* **10** 210; Nadal M H and Bourgeois L 2010 *J. Appl. Phys.* **108** 033512
[44] Gertsman V. Y. *et al.* 1994 *Acta Metall. Mater.* **42** 3539; Meyers M A and Chawla K K 2009 *Mechanical Behavior of Materials* (Cambridge: Cambridge University Press)
[45] Samsonov G. V. 1968 *Handbook of the physicochemical properties of the elements* (Plenum: New York); Bunshah R. F. and Armstrong R. W. 1969 *Mat. Res. Bull.* **4** 239
[46] Tyson W. R. and Miller W. A. 1977 *Surf. Sci.* **62** 267; Vitos L. *et al.* 1998 *Surf. Sci.* **411** 186
[47] Marcinkowski M. J. and Lipsitt H. A. 1962 *Acta Metall.* **10** 95
[48] Holzwarth U. and Stamm H. 2002 *J. Nucl. Mater.* **300** 161
[49] Mikic B. B. 1974 *Int. J. Heat Mass Transf.* **17** 205
[50] Cooper M. G., Mikic B. B. and Yovanovich M. M. 1969 *Int. J. Heat Mass Transf.* **12** 279
[51] Yovanovich M. M. 2005 *IEEE Trans. Compon. Packag. Technol.* **28** 182
[52] Pullen J. and Williamson J. B. P. 1972 *Proc. Royal Soc. A* **327** 159
[53] Nieman G. W., Weertman J. R. and Siegel R. W. 1989 *Scripta metallurgica* **23** 2013
[54] Tabor D. 1951 *The Hardness of Metals* (Clarendon Press: Oxford)
[55] Tolias P. 2017 *Nucl. Mater. Energy* **13** 42
[56] Gunn J. P. *et al.* 2017 *Nucl. Fusion* **57** 046025
[57] Rohde V. *et al.* 2003 *J. Nucl. Mater.* **313-316** 337
[58] Matyash K. *et al.* 2005 *J. Nucl. Mater.* **337-339** 237
[59] Ho C. Y., Powell R. W. and Liley P. E. 1972 *J. Phys. Chem. Ref. Data* **1** 279; Alcock C. B., Chase M. W. and Itkin V. 1993 *J. Phys. Chem. Ref. Data* **22** 1
[60] White G. K. and Collocott S. J. 1984 *J. Phys. Chem. Ref. Data* **13** 1251; White G. K. and Minges M. L. 1997 *Int. J. Thermophys.* **18** 1269
[61] Chase M. W. 1998 *J. Phys. Chem. Ref. Data Monogr.* **9** 1; Dubrovinskaia N. A. *et al.* 1997 *Calphad* **21** 497
[62] Meyer H. *et al.* 2017 *Nucl. Fusion* **57** 102014